Nanoshell-mediated near-infrared thermal therapy of tumors under magnetic resonance guidance

L. R. Hirsch*, R. J. Stafford†, J. A. Bankson†, S. R. Sershen*, B. Rivera‡, R. E. Price‡, J. D. Hazle†, N. J. Halas§, and J. L. West*¶

*Department of Bioengineering, Rice University, P.O. Box 1892, MS-142, Houston, TX 77251-1892; Departments of †Diagnostic Imaging Physics and ‡Veterinary Medicine, University of Texas M. D. Anderson Cancer Center, Houston, TX 77030; and §Department of Electrical and Computer Engineering, Rice University, P.O. Box 1892, MS-366, Houston, TX 77251-1892

Edited by Mark A. Ratner, Northwestern University, Evanston, IL, and approved September 12, 2003 (received for review April 25, 2003)

Metal nanoshells are a class of nanoparticles with tunable optical resonances. In this article, an application of this technology to thermal ablative therapy for cancer is described. By tuning the nanoshells to strongly absorb light in the near infrared, where optical transmission through tissue is optimal, a distribution of nanoshells at depth in tissue can be used to deliver a therapeutic dose of heat by using moderately low exposures of extracorporeally applied near-infrared (NIR) light. Human breast carcinoma cells incubated with nanoshells *in vitro* were found to have undergone photothermally induced morbidity on exposure to NIR light (820 nm, 35 W/cm^2), as determined by using a fluorescent viability stain. Cells without nanoshells displayed no loss in viability after the same periods and conditions of NIR illumination. Likewise, *in vivo* studies under magnetic resonance guidance revealed that exposure to low doses of NIR light (820 nm, 4 W/cm^2) in solid tumors treated with metal nanoshells reached average maximum temperatures capable of inducing irreversible tissue damage ($\Delta T = 37.4 \pm 6.6$°C) within 4–6 min. Controls treated without nanoshells demonstrated significantly lower average temperatures on exposure to NIR light ($\Delta T < 10$°C). These findings demonstrated good correlation with histological findings. Tissues heated above the thermal damage threshold displayed coagulation, cell shrinkage, and loss of nuclear staining, which are indicators of irreversible thermal damage. Control tissues appeared undamaged.

Conventional surgical treatment of solid tumors is an effective therapy for the removal of well defined, accessible, primary tumors located within nonvital tissue regions. However, the high morbidity and invasive nature associated with surgical resection renders this therapy unsuitable for treatment of small, poorly defined metastases or other tumors embedded within vital regions. Thermal ablation therapies can provide a minimally invasive alternative to conventional surgical treatment of solid tumors. In addition to their minimally invasive nature, thermal therapeutic procedures are relatively simple to perform and therefore have the potential of improving recovery times, reducing complication rates and hospital stays. Thermal delivery methods that warrant investigation for local tissue ablation include laser-induced thermal therapy (1–3), microwave and radiofrequency (RF) ablation (4–6), magnetic thermal ablation (7, 8), and focused ultrasound (9).

The goal of a minimally invasive thermal ablation treatment is to conform a lethal dose of heat to the prescribed tissue volume with as little damage to intervening and surrounding normal tissue as possible. Usually, delivery is by means of interstitial or intracavity placement of catheters or probes. Externally focused ultrasound transducers have successfully provided a means by which thermal therapies can be performed extracorporeally, but the volume and speed of such treatments is limited by the potential destruction of normal tissue in the near field between the target and the ultrasound probe (10). RF and microwave therapies suffer from similar near field or intervening tissue problems. In addition, energy deposition is often much slower with these moieties, serving to increase the treatment time and generate less sharp lesion boundaries. Like RF and microwave therapies, laser-induced thermal therapy approaches suffer a common limitation, which arises from the fact that the heating from these sources is nonspecific, making the energy source the heat source. Treatment volumes and times are therefore limited by the maximum temperature near the tip and the temperature at the expanding thermal boundary. Treatment of larger volumes with this method often requires slow diffusion from the source, resulting in extended treatment times and generating poorly defined lesion boundaries. In particular, this method makes treatment of large or irregularly sized lesions with conventional laser thermal therapy impractical and somewhat difficult (3). Yet another approach uses alternating magnetic fields to heat oxide nanoparticles embedded within tissue. Unlike the techniques listed above, this magnetic thermal therapy approach provides selective heating to tissues loaded with the thermal coupling agent (iron oxide in this case). Potential limitation appears to be the high quantity of iron required to induce heating; tumors were injected with up to 10% total weight of iron oxide.

Here we present an approach to thermal therapeutics using a class of nanoparticles called metal nanoshells, which perform as intense near-infrared (NIR) absorbers. Metal nanoshells consist of a spherical dielectric core nanoparticle, in this case silica, which is surrounded by a thin metal shell, in this case gold (11, 12). These particles possess a highly tunable plasmon resonance, a resonant phenomenon whereby light induces collective oscillations of conductive metal electrons at the nanoshell surface. The particle's plasmon resonance, in turn, determines the absorbing and scattering properties of the particle. Whereas many bulk metals demonstrate plasmon resonance behavior, they do so over a very small region of the visible spectrum. Unique to nanoshells is their plasmon tunability, as well as the ease and controllability by which the tunability is achieved. By controlling the relative thickness of the core and shell layers of the nanoparticle, the plasmon resonance and the resultant optical absorption of nanoshells can be tuned across a broad region of the spectrum from the near-UV to the midinfrared. This range spans the NIR (13), a region where optical absorption in tissue is minimal and penetration is optimal (14). To date, nanoshells have demonstrated their usefulness in applications ranging from photooxidation inhibition in photoluminescent polymer films (15), Raman sensors that can be optimized to specific pump laser wavelengths (16, 17), substrates for whole-blood biosensing (18), optically triggered drug delivery (19), and optomechanical materials (20, 21).

In this article, we used silica–gold nanoshells with a strong absorption in the NIR. As an NIR absorber, nanoshells are optically very robust; the nanoshell's rigid structure and noble

This paper was submitted directly (Track II) to the PNAS office.

Abbreviations: NIR, near-infrared; MR, magnetic resonance; MRTI, MR temperature imaging; PEG, polyethylene glycol; SH-PEG, thiolated PEG.

¶To whom correspondence should be addressed. E-mail: jwest@rice.edu.

metal surface make it far less susceptible to chemical/thermal denaturation and photobleaching effects than conventional NIR dyes (22), providing extended performance *in situ*. Nanoshells are also intense absorbers. Conventional NIR dyes like Indocyanine green possess an absorption cross section of $\approx 1.66 \times 10^{-20}$ m^2 at wavelengths $\approx$800 nm; in contrast, Mie scattering theory predicts that the metal nanoshells used in the following study possess absorption cross sections on the order of 3.8×10^{-14} m^2. This finding implies that a nanoshell is over 1 million-fold more likely than the comparable dye to encounter an absorbing event and convert that light into thermal energy. Nonetheless, pioneering work by Chen *et al.* (23–25) investigated Indocyanine green as a thermal coupling agent delivered intratumorally into tumor tissue with moderate success. A further benefit of nanoshells versus conventional dyes is the potential to both "stealth" the nanoshells with immunoinert materials as well as conjugate them with biomolecules for targeted therapy after systemic delivery (26, 27). This result is accomplished through the nanoshell's gold surface. An otherwise inert and biocompatible material (28), the gold surface provides simple chemistry for the self-assembly of polyethylene glycol (PEG), antibodies, or a variety of other agents. Conventional organic dyes, on the other hand, often lack available chemical moieties for facile conjugation of such compounds, resulting in shorter circulation times.

The therapeutic strategy reported here exploits the naturally occurring deficit of NIR-absorbing chromophores in most tissue, permitting transmission of NIR light (700–1,000 nm) through tissue with scattering-limited attenuation and minimal heating. Light within this spectral region has been shown to penetrate tissue at depths beyond 1 cm with no observable damage to the intervening tissue (29). Numerous medical diagnostic applications have taken advantage of the deep-penetrating, benign nature of NIR radiation, including pulse oximetry (30), optical coherence tomography (31), diffuse tomography (32), and laser Doppler imaging (31, 33, 34). Combining these two otherwise benign moieties (nanoshells and NIR light), we present a technique that allows a noninvasive delivery of heat to a tissue volume by using an extracorporeal, low-power diode laser to selectively induce photothermal destruction of a tumor volume treated with gold nanoshell particles. Furthermore, we believe that real-time magnetic resonance temperature imaging (MRTI) monitoring, in combination with the intense NIR-absorbing, nonbleaching, easily conjugable nanoshells, facilitates the potential for a minimally invasive NIR-based thermal ablation therapy and may bring targeted NIR therapeutics to the forefront as a viable, minimally invasive method of cancer treatment.

Materials and Methods

Synthesis of Thiolated PEG (SH-PEG). SH-PEG was synthesized by reacting PEG-amine (M_r 5,000, Nektar, Huntsville, AL) with 2-iminothiolane (Sigma-Aldrich) for 1 h. The product was then dialyzed (molecular weight cutoff of 500; Spectrum Laboratories, Rancho Domingo, CA) against deionized (DI) H_2O for at least 4 h to remove excess reagent. The SH-PEG yield was determined colorimetrically at 412 nm after reacting with Ellman's reagent, 5,5′-dithio-bis(2-nitrobenzoic acid), from Sigma. Product was stored at −20°C.

Gold–Silica Nanoshell Fabrication. Metal nanoshells were fabricated as described (11). Briefly, silica nanoparticles were grown by the Stöber method (35), in which tetraethyl orthosilicate (Aldrich) was reduced in NH_4OH in ethanol. Particles were sized with a Philips XL30 scanning electron microscope; polydispersity of <10% was considered acceptable. The particle surface was then terminated with amine groups by reaction with aminopropyltriethoxysilane (Aldrich) in ethanol.

Very small gold colloid (1–3 nm) was grown by using the method of Duff and Baiker (36). This colloid was aged for 2 weeks at 4°C and was then concentrated by using a rotary evaporator. Aminated silica particles were then added to the gold colloid suspension. Gold colloid adsorbs to the amine groups on the silica surface, resulting in a silica nanoparticle covered with gold colloid. Gold–silica nanoshells were then grown by reacting $HAuCl_4$ with the silica-colloid particles in the presence of formaldehyde. This process reduces additional gold onto the adsorbed colloid, which act as nucleation sites, causing the surface colloid to grow and coalesce with neighboring colloid, forming a complete metal shell. Nanoshell formation was assessed by using a U-2001 UV-Vis spectrophotometer (Hitachi, Tokyo) and scanning electron microscopy. Nanoshells were designed to have a 55-nm core radius and a 10-nm-thick shell to have a peak absorption in the NIR (13).

SH-PEG was assembled onto nanoshell surfaces by combining 5 μM SH-PEG and 1.5×10^{10} nanoshells per ml in DI H_2O for 1 h, followed by centrifugation and resuspension in DI H_2O. Before injection, nanoshells were suspended in PBS (PBS/100 mM Na_2HPO_4/150 mM NaCl, pH 7.4). Colloid stability in saline was monitored through spectrophotometric analysis at the nanoparticles' peak absorbance.

***In Vitro* Photothermal Nanoshell Therapy.** Human breast epithelial carcinoma SK-BR-3 cells (ATCC) were cultured in 12-well plates in McCoy's 5a modified medium supplemented with FBS (10% vol/vol), glutamine (1.9 mM), penicillin (88 units/ml), and streptomycin (88 μg/ml).

Nanoshells were suspended in serum-free medium (4.4×10^9 particles per ml). Cells were rinsed with PBS and incubated with nanoshells at 37°C. Nanoshell-free control treatments received only serum-free medium. After 1 h, excess unbound nanoshells were removed by rinsing three times with PBS. Fresh culture medium was then added to the wells.

Cells were exposed to NIR light (coherent, 820 nm, 35 W/cm^2) for 7 min to induce photothermal cell damage. After exposure to light, cells were incubated for an additional 2 h at 37°C. The cells were then exposed to three different stains that identify (*i*) cell viability, (*ii*) membrane permeability/damage, and (*iii*) nanoshell binding. Cell viability was assessed by using calcein AM (Molecular Probes, 1 μM), which causes viable cells to fluoresce green. Cell membrane damage was identified by using an aldehyde-fixable fluorescein dextran dye (M_r 10,000, Molecular Probes). Cells were incubated with the fluorescent dextran for 30 min, rinsed once, and quickly fixed with 5% glutaraldehyde. To evaluate cellular binding of nanoshells, cells were fixed in 2.5% glutaraldehyde for 10 min, rinsed three times with DI H_2O, and exposed to a silver enhancement stain (Amersham Pharmacia) for analysis of nanoshell binding through phase contrast microscopy.

Transmissible Venereal Tumor (TVT) Tumor Inoculation. Female nonobese diabetic CB17-Prkd c SCID/J mice were handled in accordance with the Institutional Animal Care and Use Committee of the University of Texas M. D. Anderson Cancer Center. Canine TVT cells (courtesy of A. Harmelin, The Weizmann Institute of Science, Rehovot, Israel) were inoculated s.c. ($\approx$0.25 ml) into the right and left hind leg of each mouse (n = 5) and grown to a tumor burden of $\approx$1.0 cm in diameter (usually $\approx$6 weeks).

***In Vivo* Nanoshell Therapy.** Mice were anesthetized with isoflurane, and the skin over the tumor was shaved and swabbed with PEG diacrylate (M_r 600, Sartomer, West Chester, PA) as an index-matching agent. PEG-passivated NIR-absorbing gold–silica nanoshells (20–50 μl) were injected interstitially $\approx$5 mm into the tumor volume. Control tumor sites received a saline injection. Five to 30 min after injection, tumor sites were exposed to NIR light (820 nm, 4 W/cm^2, 5-mm spot diameter, <6 min), whereas

temperature profiles were monitored by using phase-sensitive, fast-spoiled gradient-echo MRI.

MRI was used for treatment planning, localization, and monitoring of the temperature distribution during the treatments. All imaging studies were performed in a 1.5-T MR scanner (Signa Echospeed, General Electric Medical Systems, Milwaukee, WI) equipped with high-performance gradients (23 mT/m maximum amplitude and 120 T per m per sec maximum slew rate) and fast receiver hardware (bandwidth, ±500 MHz). Mice were placed on a 3-in (1 in = 2.54 cm) receive-only surface coil specially designed for small animal imaging (courtesy of R. Giaquinto, General Electric Corporate Research and Development, Schenectady, NY). T1- and T2-weighted images were used to plan and localize the treatment by verifying the position of the laser fiber relative to the imaged region before irradiation. MRTI was performed by using a complex phase-difference technique with a fast, 2-D RF-spoiled gradient-recalled echo sequence (TR/TE = 49.5 ms/20 ms, flip angle = 30°, bandwidth = 9.62 kHz). To achieve a 5 sec per image scan time for the small field of view (4×2 cm^2), partial Fourier imaging in the phase-encode direction (256×48 encoding matrix) with phase-preserving reconstruction was used along with a reduced bandwidth to minimize gradient heating limitations. The acquired voxel size was $0.16 \times 0.31 \times 3$ mm^3. The in-plane resolution was interpolated to a 0.16×0.16 mm^2 pixel size by using zero padding before extrapolation of the temperature data. The change in temperature from baseline after N images (ΔT_N) was extrapolated from the complex-valued MRTI data (S) by using the temperature dependence of the proton resonance frequency shift (37) and an assumed temperature sensitivity (α) of -0.01 ppm/°C according to the relation in Eq. **1**

$$\Delta T_N = \sum_{i=1}^{N} \delta T_i = \frac{\sum_{i=1}^{N} \delta\phi_i}{2\pi \cdot \gamma B_0 \cdot \alpha \cdot TE} = \frac{\sum_{i=1}^{N} \arg(S^*_{i-1} S_i)}{2\pi \cdot \gamma B_0 \cdot \alpha \cdot TE}, \qquad [1]$$

where δT_i is the temperature difference measured between the i and (i–1) images, γB_0 is the resonance frequency (63.87 MHz), and TE is the sequence echo time (38). Thermal dose was calculated in equivalent minutes at 43°C (t_{43}) by using the relationship in Eq. **2**

$$(t_{43})_N = \sum_{i=1}^{N} R^{(43°C - T_i)} \cdot \Delta t, \quad \text{with } R = \begin{cases} 0.25, & T_i < 43°C \\ 0.50, & T_i \geq 43°C, \end{cases} \qquad [2]$$

where Δt is the time between measurements (in this case the time between images), T_i is the temperature in degrees Celsius for the ith measurement, and R is a constant empirically derived from hyperthermia experiments in living tissue (39). Temperature and dose information were calculated and made available for display on the scanner during the treatments by using software developed inhouse in the FUNCTOOL V. 1.9 environment (Advantage Windows Workstation, General Electric Medical Systems, Waukesha, WI). Offline data processing, including color overlays and plotting, was performed by using code developed in the MATLAB environment (Mathworks, Natick, MA).

Tumor excision and fixation proceeded immediately after treatment and euthanasia. Histological evaluation was conducted by means of hematoxylin/eosin and silver enhancement staining of paraffin-embedded tissue sections to assess the distribution of tissue damage and nanoshells, respectively, within the treatment area. MRI thermal data were then compared with images from gross pathology and histology of tumor sections.

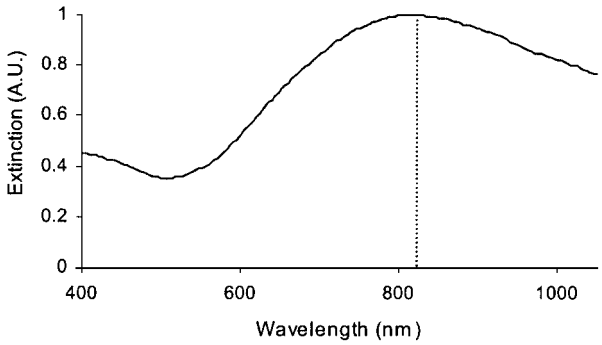

Fig. 1. Extinction spectrum of nanoshells in water confirms the overlap of peak nanoshell absorbance with the emission wavelength (820 nm) of the laser source (dotted line), promoting optimal laser-induced nanoshell heating.

Results and Discussion

NIR-absorbing nanoshells were fabricated with a 110 ± 11-nm-diameter core and a 10-nm-thick gold shell resulting in a peak absorbance at 820 nm, matching the emission wavelength of the diode laser (Fig. 1). PEG passivation of gold nanoshell surfaces was performed to minimize aggregation in physiological environments. Assembling a monolayer of PEG onto the surface introduces a brush border of sterically stabilizing polymer on the nanoparticle surface. Spectrophotometric analysis revealed a <10% reduction in the nanoshells' peak absorbance after suspension in saline. Spectral broadening, redshifting, and reduction of the original absorbance peak are indicators of colloidal aggregation, which is a behavior typical of metal colloids suspended in saline solutions. Little of this behavior is seen with the PEG-passivated nanoshells, confirming successful retention of nanoshell colloidal stability using PEG.

Localized photothermal destruction of carcinoma cells has been demonstrated *in vitro*. Silver staining of nanoshell-treated SK-BR-3 cells revealed that the protein-adsorbent gold surface of bare nanoshells promoted high densities of nanoshell binding to the cells. Nanoshell-free controls demonstrated no silver staining. On laser exposure at 35 W/cm^2 for 7 min, all nanoshell-treated samples underwent photothermal destruction within the laser spot as determined by calcein AM viability staining (Fig. 2). Circular regions of cell death are seen in fluorescence microscopy images. The diameters of these regions match the laser spot size, confirming that cell death was confined to the laser/nanoshell treatment area. Exposing the cells to either nanoshells or NIR light individually did not compromise cell viability.

In addition to loss in viability, cells receiving nanoshell/laser treatments underwent sufficient damage to irreversibly compromise cell membrane barriers. Effectively impermeable to healthy cells, the M_r 10,000 fluorescent dextran dye clearly penetrated the intracellular space of nanoshell/laser-treated cells (Fig. 2) over the same circular-sized area as the viability stain. Like the viability results, membrane permeability was not compromised in either of the controls. These findings do not suggest the causality of cell death, only an associated loss in membrane integrity with the loss of cell viability in this therapeutic regime.

In vivo MRTI analysis revealed that nanoshell-treated tumors resulted in an average temperature increase of 37.4 ± 6.6°C on NIR exposure for 4–6 min. This therapy raised temperatures well above the damage threshold necessary to induce irreversible tissue damage (40) and did so by using laser dosages that were 10- to 25-fold less than those used in earlier studies examining Indocyanine green dye (24). Meanwhile, nanoshell-free controls treated for the same period saw average temperature increases of 9.1 ± 4.7°C, levels that are insufficient to induce irreversible

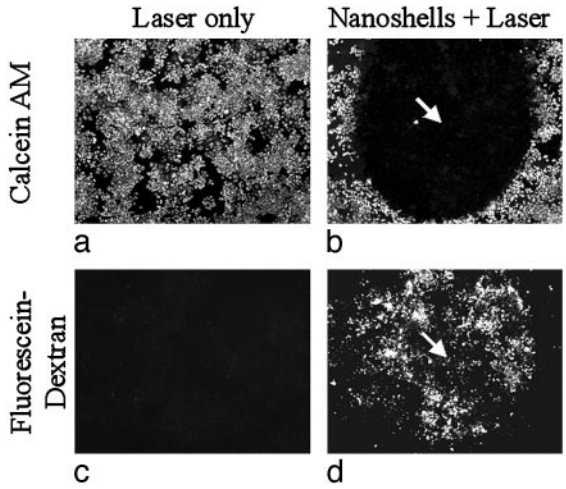

Fig. 2. Cells irradiated in the absence of nanoshells maintained both viability, as depicted by calcein fluorescence (*a*), and membrane integrity, as indicated by lack of intracellular fluoroscein dextran uptake (*c*). Cells irradiated with nanoshells possess well defined circular zones of cell death in the calcein AM study (*b*) and cellular uptake of fluoroscein dextran from increased membrane permeability (*d*).

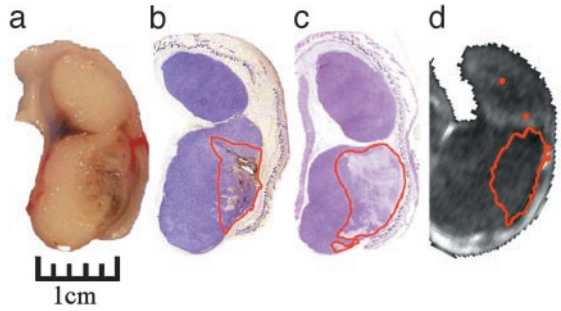

Fig. 3. (*a*) Gross pathology after *in vivo* treatment with nanoshells and NIR laser reveal hemorrhaging and loss of tissue birefringence beneath the apical tissue surface. (*b*) Silver staining of a tissue section reveals the region of localized nanoshells (outlined in red). (*c*) Hematoxylin/eosin staining within the same plane clearly shows tissue damage within the area occupied by nanoshells. (*d*) Likewise, MRTI calculations reveal an area of irreversible thermal damage of similar dimension to *a*, *b*, and *c*.

tissue damage. The average temperature increases reported here were acquired at a depth of ≈2.5 mm beneath the dermal surface over a 2 × 2 pixel area, or roughly 0.32 × 0.32 mm. All measurements exclude the highest and lowest temperature readings from each sample in an attempt to eliminate outlier artifacts that can arise from movement or drying at the tissue surface. The noise, or the spatial SD in the background of the temperature difference images, was low and did not exceed 1.5°C in any of the images. A complete list of the average temperature elevation from each study is reported in Table 1. Observed variances in the maximum temperature change were likely due to intraexperimental perturbations in the distribution of the nanoshells within the treatment volume (particularly distance from skin surface), the angle of incidence, and source-to-skin distance of the laser fiber, as well as the placement of the MR plane for observation. In the one outlier where temperatures reached 60°C, the maximum was found very close to the skin surface (<1 mm) and may have been the result of accidental deposition of a small nanoshell volume onto the outer dermal surface after injection.

Overall, these findings correlated well with gross pathology, in which defined zones of edema and loss of birefringence were observed in some of the nanoshell-treated tumors in the regions where MRTI suggested there should be irreversible tissue damage. Histology also identified common markers of thermal damage in NIR/nanoshell-treated tumors, such as coagulation, cell shrinkage, and loss of nuclear staining (Fig. 3). Within regions of thermal damage, nanoshells were found by using a sliver enhancement stain that amplifies the size of the nanoparticles for examination by optical microscopy. Despite the local injection of nanoshells 5 mm into the tumor, nanoshells were found to diffuse easily throughout the tumor. During nanoshell injection, the tumor surface quickly turns a visible greenish color common to nanoshells. Histology also confirmed a diffuse distribution of nanoshell over a large volume within the tumor, all of which suggests that the nanoparticles' small diameter of 130 nm permits diffusion from the injection site throughout the interstitium. The diffuse distribution explains why heating does not initiate 5 mm below the surface at the injection site, but instead heats with a profile that mimics a volume containing a nearly uniform distribution of absorbing material. Whereas heating above damage threshold was seen for all experimental samples, neither the irradiated saline controls nor treatments receiving nanoshell injections without irradiation provided any visible tissue damage in gross pathology or histology. Although histology and MRTI analysis both confirm tissue damage in nanoshell treatments, discrepancies exist in zonal depth of tissue damage assessed by histopathology and MRI analysis, which may be attributed to misregistration of the imaging plane with the histological sections.

Table 1. Average tumor heating in nanoshell-treated and nanoshell-free controls

	$\Delta T \pm$ SD	
Mouse	Control	Nanoshell
1	4.7 ± 0.7	39.7 ± 4.7
2	8.4 ± 1.6	60.4 ± 3.4
3	9.1 ± 2.5	44.6 ± 6.0
4	5.9 ± 1.2	32.8 ± 1.2
5	8.7 ± 0.9	28.1 ± 1.0
6	7.6 ± 1.6	32.5 ± 0.7

Further examination of thermal profiles as a function of depth (Fig. 4) reveal a profile in good qualitative agreement with theoretical and experimental data published elsewhere (41, 42). Maximal temperature changes were found to occur ≈1 mm beneath the apical surface. This behavior may be the product of higher photon densities in this region, which is a phenomenon often seen in highly scattering mediums like tissue. The additional contributions from backscattered light coming from other depths can create subdermal light dosages exceeding the original dosage by as much as 140% (42). In addition to this effect, convective cooling at the air–tissue interface will also promote cooler surface temperatures. Regardless of cause, the end result is a zone of thermal damage spanning a depth of ≈4 mm after 6 min. This limit of damage depth may be due to a variety of factors. As with conventional thermal therapies, some maximal treatment volume will exist for nanoshell thermal therapy, and although nanoshell densities do begin to diminish at these depths, we do not attribute this falloff in heating to reduced concentrations of nanoshells. A more likely contributor to this falloff is reduced NIR intensities due to both scattering from tissue and absorption from upperlying nanoshells. Although maximal depths of treatment appear to be ≈4–6 mm for this setup, we can report that heating has been observed at depths beyond 1 cm in other studies. Even greater depths may be achievable by combining lower nanoshell concentrations (providing deeper NIR penetration into the tumor) with extended

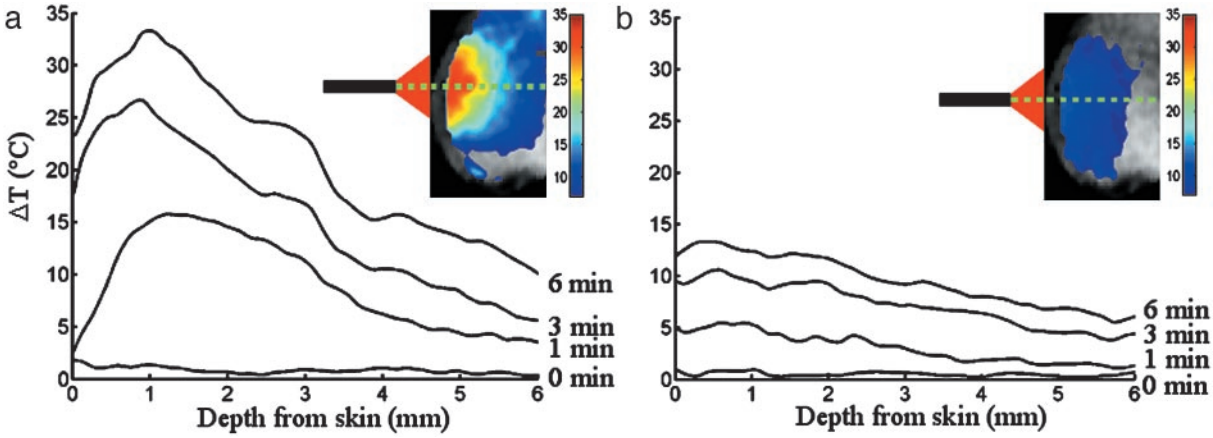

Fig. 4. Measured temperature rise plotted as a function of depth along the trajectory. Measured temperature rise in a region of interest at 0, 1, 3, and 6 min for nanoshell treatment (*a*) and control treatment (*b*).

irradiation times or higher laser powers. The maximum treatable depth will also be tissue-specific, as the scattering, perfusion, and pigmentation between tissues differ, resulting in varying background attenuation between tissue. Whereas no natural pigments absorb strongly in the NIR, many absorb to some extent (14). At sufficient concentration and laser powers, the presence of these pigments may reduce the maximum laser dosage tolerable in healthy tissue due to the increased background tissue heating from the absorbing pigment.

Fig. 5 demonstrates temperature change versus time for several depths (2.5, 3.75, 5.0, and 7.3 mm) within the tumor during treatment. Heating occurs in two phases: initial rapid transient heating, followed by a gradual heating until the laser is turned off. The first phase of heating occurs during the first minute of irradiation. We speculate that such a significant degree of heating within a brief period is due to intense localized heating before thermal relaxation into surrounding tissue takes hold. This finding suggests that alternative dosage regimens (higher dosage, less exposure time) may provide improved heating while minimizing heating in surrounding tissue. Cooling, meanwhile, proceeded with predictable Newtonian behavior.

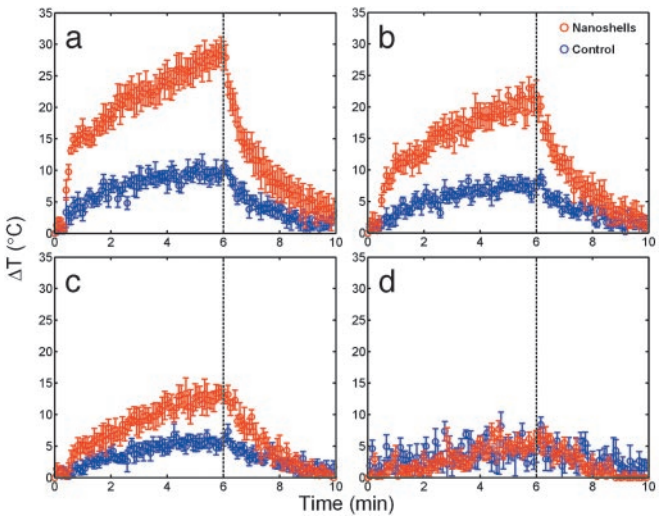

Fig. 5. Temporal plots of maximum temperature change of NIR-irradiated tumors with nanoshells (red) and without nanoshells (blue) at depths of 2.5 (*a*), 3.75 (*b*), 5.0 (*c*), and 7.3 (*d*) mm beneath the apical tissue surface.

Now that a regime of nanoshell and laser dosage has been found for successful therapy of nanoshell-treated tumors, survival studies monitoring tumor growth/regression of entire tumors after treatment with the NIR nanoshell therapy under MR guidance are possible. Future investigations of a targeted nanoshell therapy that is similar in many ways to the delivery of stealth liposomes (43, 44) are warranted, where nanoshells are "stealthed" with PEG, systemically injected, and preferentially accumulated at the tumor site due to the highly permeable, poorly organized vascular networks commonly found in neoplastic tumors. This preferential accumulation behavior is often referred to as the enhanced permeability and retention effect (45). NIR treatment of the bulk tissue then selectively heats and destroys the nanoshell-laden tumor regions within the tissue, while leaving surrounding tissue intact. As an additional adjuvant, nanoshells may also be conjugated with antibodies targeting surface oncoproteins overexpressed within the tumor to promote cell internalization, further accumulation, and more selective thermal damage of the tumor. Such therapies could have a large impact on the treatment of secondary metastases and other tumors considered to be otherwise inoperable.

Conclusions

By using two benign moieties (NIR light and nanoshells) we have successfully achieved localized, irreversible photothermal ablation of tumor tissue both *in vitro* and *in vivo*. *In vitro*, cells irradiated with very high dosages of NIR laser without nanoshells maintained viability. Likewise, cells incubated with nanoshells in the absence of laser maintained viability as well, suggesting that neither therapy by itself is cytotoxic. Combining these two therapies, however, produced localized cell death confined to the laser/nanoshell treatment area. Similar results were seen *in vivo*. With the aid of MRTI, real-time thermal monitoring of tumors treated with the intense NIR-absorbing, nonbleaching nanoshells ensured that successful irreversible thermal destruction was achieved and confined to the tumor volume. Furthermore, histological examination revealed that MRTI estimation of tissue damage was in good agreement with experimental findings, demonstrating its potential utility in determining tissue damage during therapy, making it possible to tailor therapy regimens to ensure the complete thermal destruction of tumors in future studies.

We thank the National Science Foundation (Award EEC-0118007) for its support of the Center for Biological and Environmental Nanotechnology (Rice University, Houston). This work also was supported by a research grant from the Charles E. Culpeper Biomedical Pilot Initiative.

1. Amin, Z., Donald, J. J., Masters, A., Kant, R., Steger, A. C., Bown, S. G. & Lees, W. R. (1993) *Radiology (Easton, Pa.)* **187,** 339–347.
2. Nolsøe, C. P., Torp-Pedersen, S., Burcharth, F., Horn, T., Pedersen, S., Christensen, N. E., Olldag, E. S., Andersen, P. H., Karstrup, S., Lorentzen, T., *et al.* (1993) *Radiology (Easton, Pa.)* **187,** 333–337.
3. Vogl, T. J., Mack, M. G., Müller, P. K., Straub, R., Engelmann, K. & Eichler, K. (1999) *Eur. Radiol.* **9,** 1479–1487.
4. Seki, T., Wakabayashi, M., Nakagawa, T., Imamura, M., Tamai, T., Nishimura, A., Yamashiki, N., Okamura, A. & Inoue, K. (1999) *Cancer (Philadelphia)* **85,** 1694–1702.
5. Gazelle, G. S., Goldberg, S. N., Solbiati, L. & Livraghi, T. (2000) *Radiology (Easton, Pa.)* **217,** 633–646.
6. Mirza, A. N., Fornage, B. D., Sneige, N., Kuerer, H. M., Newman, L. A., Ames, F. C. & Singletary, S. E. (2001) *Cancer J.* **7,** 95–102.
7. Hilger, I., Andrä, W., Bähring, R., Daum, A., Hergt, R. & Kaiser, W. A. (1997) *Invest. Radiol.* **32,** 705–712.
8. Hilger, I., Hiergeist, R., Hergt, R., Winnefeld, K., Schubert, H. & Kaiser, W. (2002) *Invest. Radiol.* **37,** 580–586.
9. Jolesz, F. A. & Hynynen, K. (2002) *Cancer J.* **8,** S100–S112.
10. Köhrmann, K. U., Michel, M. S., Gaa, J., Marlinghaus, E. & Alken, P. (2002) *J. Urol.* **167,** 2397–2403.
11. Oldenberg, S. J., Averitt, R. D., Westcott, S. L. & Halas, N. J. (1998) *Chem. Phys. Lett.* **28,** 243–247.
12. Averitt, R. D., Westcott, S. L. & Halas, N. J. (1999) *J. Opt. Soc. Am. B* **16,** 1824–1832.
13. Oldenburg, S. J., Jackson, J. B., Westcott, S. L. & Halas, N. J. (1999) *Appl. Phys. Lett.* **75,** 2897–2899.
14. Weissleder, R. (2001) *Nat. Biotechnol.* **19,** 316–317.
15. Hale, G. D., Jackson, J. B., Lee, T. R. & Halas, N. J. (2000) *Appl. Phys. Lett.* **78,** 1502–1504.
16. Oldenberg, S. J., Westcott, S. L., Averitt, R. D. & Halas, N. J. (1999) *J. Chem. Phys.* **111,** 4729–4735.
17. Jackson, J. B., Westcott, S. L., Hirsch, L. R., West, J. L. & Halas, N. J. (2003) *Appl. Phys. Lett.* **82,** 257–259.
18. Hirsch, L. R., Jackson, J. B., Lee, A., Halas, N. J. & West, J. L. (2003) *Anal. Chem.* **75,** 2377–2381.
19. Sershen, S. R., Westcott, S. L., Halas, N. J. & West, J. L. (2000) *J. Biomed. Mater. Res.* **51,** 293–298.
20. Sershen, S. R., Westcott, S. L., Halas, N. J. & West, J. L. (2002) *Appl. Phys. Lett.* **80,** 4609–4611.
21. Sershen, S. R., Westcott, J. L., West, J. L. & Halas, N. J. (2001) *Appl. Phys. B* **73,** 379–381.
22. Landsman, M. L. J., Kwant, G., Mook, G. A. & Zijlstra, W. G. (1976) *J. Appl. Physiol.* **40,** 575–583.
23. Chen, W. R., Adams, R. L., Bartels, K. E. & Nordquist, R. E. (1995) *Cancer Lett. (Shannon, Irel.)* **94,** 125–131.
24. Chen, W. R., Adams, R. L., Higgins, A. K., Bartels, K. E. & Nordquist, R. E. (1996) *Cancer Lett. (Shannon, Irel.)* **98,** 169–173.
25. Chen, W. R., Adams, R. L., Carubelli, R. & Nordquist, R. E. (1997) *Cancer Lett. (Shannon, Irel.)* **115,** 25–30.
26. Karyakin, A. A., Presnova, G. V., Rubtsova, M. Y. & Egorov, A. M. (2000) *Anal. Chem.* **72,** 3805–3811.
27. Yang, M. S., Yau, H. C. M. & Chan, H. L. (1998) *Langmuir* **14,** 6121–6129.
28. Tang, L., Liu, L. & Elwing, H. (1998) *J. Biomed. Mater. Res.* **41,** 333–340.
29. Shah, N., Cerussi, A., Eker, C., Espinoza, J., Butler, J., Fishkin, J., Hornung, R. & Tromberg, B. (2001) *Proc. Natl. Acad. Sci. USA* **98,** 4420–4425.
30. Nakajimi, S., Hirai, H., Takase, H., Kuze, A. & Aoyagi, S. (1975) *Kokyu To Junkan* **23,** 709–713.
31. Huang, D., Swanson, E. A., Lin, C. P., Schuman, J. S., Stinson, W. G., Chang, W., Hee, M. R., Flotte, T., Gregory, K., Puliafito, C. A. & Fujimoto, J. G. (1991) *Science* **254,** 1178–1181.
32. Ntziachristos, V., Tung, C. H., Bremer, C. & Weissleder, R. (2002) *Nat. Med.* **8,** 757–760.
33. Forrester, K., Doschak, M. & Bray, R. (1997) *Med. Biol. Eng. Comput.* **35,** 581–586.
34. Pogue, B. W., Willscher, C., McBride, T. O., Osterberg, U. L. & Paulsen, K. D. (2000) *Med. Phys.* **27,** 2693–2700.
35. Stober, W. & Fink, A. (1968) *J. Colloid Interface Sci.* **26,** 62–69.
36. Duff, D. G. & Baiker, A. (1993) *Langmuir* **9,** 2301–2309.
37. Hindman, J. C. (1966) *J. Chem. Phys.* **44,** 4582–4592.
38. Ishihara, Y., Calderon, A., Watanabe, H., Okamoto, K., Suzuki, Y., Kuroda, K. & Suzuki, Y. (1995) *Magn. Reson. Med.* **34,** 814–823.
39. Sapareto, S. A. & Dewey, W. C. (1984) *Int. J. Radiat. Oncol. Biol. Phys.* **10,** 787–800.
40. Pearce, J. & Thomsen, S. (1995) in *Optical-Thermal Response of Laser-Irradiated Tissue*, eds. Welch, A. & Gemert, M. V. (Plenum, New York), pp. 561–604.
41. Flock, S. T., Patterson, M. S., Wilson, B. C. & Wyman, D. R. (1989) *IEEE Trans. Biomed. Eng.* **36,** 1162–1168.
42. Jacques, S. L. (1989) *Cancer Bull.* **41,** 211–218.
43. Wu, N. Z., Da, D., Rudoll, T. L., Needham, D., Whorton, A. R. & Dewhirst, M. W. (1993) *Cancer Res.* **53,** 3765–3770.
44. Papahadjopoulos, D., Allen, T. M., Gabizon, A., Mayhew, E., Matthay, K., Huang, S. K., Lee, K. D., Woodle, M. C., Lasic, D. D., Redemann, C. & Martin, F. J. (1991) *Proc. Natl. Acad. Sci. USA* **88,** 11460–11464.
45. Maeda, H. (2001) *Adv. Enzyme Regul.* **41,** 189–207.